nature communications

Article

https://doi.org/10.1038/s41467-025-56831-9

Kosmotropic aqueous processing solution for green lithium battery cathode manufacturing

Received: 7 March 2024

Accepted: 29 January 2025

Published online: 16 February 2025

Check for updates

Jung-Hui Kim[1,6], Won-Yeong Kim[1,6], Sebin Kim[2,6], Jeongdong Kim[1], Seok-Ju Lee[1], Namjun Park[2], Sun-Phil Han[3], Kun Ryu[4], Junghwan Kim[1] ✉, Won Bo Lee[2] ✉ & Sang-Young Lee[1,5] ✉

The global pursuit of carbon neutrality is driving efforts toward environmentally friendly aqueous electrode manufacturing. However, the inherent chemical reactivity of water with cathode materials remains a challenge to achieving this goal. Here, we design a class of aqueous processing solutions based on the kosmotropic effect. Ion hydration shells in the kosmotropic solutions are restructured to form an ordered state of anion–water clusters and to stabilize local hydration structure adjacent to cathode materials. Consequently, interfacial side reactions and structural degradation of Ni-rich cathode materials are mitigated. The kosmotropic solution-processed $LiNi_{0.8}Co_{0.1}Mn_{0.1}O_2$ cathode achieve high specific and areal capacities (≥ 205 mAh g^{-1} and ≥ 3.7 mAh cm^{-2}) together with stable cyclability, which are comparable to those of commercial *N*-methyl-2-pyrrolidone (NMP)-processed cathodes. Techno-economic analysis demonstrates that this kosmotropic solution approach reduces energy consumption in battery manufacturing by 46% compared to the NMP-based process, highlighting its practical and sustainable viability.

Advancements in clean energy storage are crucial for accelerating the transition to a sustainable future. Lithium-ion batteries (LIBs) are widely favored for their high energy density, long cycle life, and balanced electrochemical properties[1]. To continuously meet the ever-increasing demand for high energy density, LIBs favor the utilization of transition metal (TM) oxide-based cathode materials ($Li_xM_yO_z$: M = Ni, Co, and Mn), which are optimized for high-capacity and high-voltage operations. However, the current manufacturing process for energy-dense battery cathodes uses *N*-methyl-2-pyrrolidone (NMP). This teratogenic and toxic processing solvent is classified as a Substance of Very High Concern (SVHC) under the European Union Registration, Evaluation, Authorization, and Restriction of Chemicals (REACH) regulation[2]. Environmental and safety concerns surrounding the NMP solvent have prompted efforts to reduce and ultimately eliminate its use. This issue was further highlighted by the European battery regulation (2023/1542), which was announced in June 2023 with the common goal of minimizing the harmful effects of batteries on the environment. A dry-coating process, which does not utilize processing solvents, has been proposed as a promising approach to address this issue. However, its lack of compatibility with current commercial wet-based electrode production lines hinders its practical implementation in the near future[3]. Therefore, an urgent transition to scalable cathode manufacturing using environmentally benign processing solvents, which should also be compatible with existing electrode fabrication

[1]Department of Chemical and Biomolecular Engineering, Yonsei University, Seoul, Republic of Korea. [2]School of Chemical and Biological Engineering, Institute of Chemical Processes, Seoul National University, Seoul, Republic of Korea. [3]UNIST Central Research Facilities, Ulsan National Institute of Science and Technology (UNIST), Ulsan, Republic of Korea. [4]Pritzker School of Molecular Engineering, The University of Chicago, Chicago, IL, USA. [5]Department of Battery Engineering, Yonsei University, Seoul, Republic of Korea. [6]These authors contributed equally: Jung-Hui Kim, Won-Yeong Kim, Sebin Kim.
✉e-mail: kjh24@yonsei.ac.kr; wblee@snu.ac.kr; syleek@yonsei.ac.kr

processes, is essential to comply with environmental regulations and ensure sustainable battery production.

Water, the greenest substance on Earth (Supplementary Fig. 1), offers a promising solution to the challenges above and exhibits advantages for cathode production, including its innate ubiquity, environmental friendliness, and potential for ease of recycling due to the use of water-soluble electrode binders (compared to organic solvent-soluble fluorine binders)[4]. Nonetheless, certain challenges are associated with the aqueous cathode manufacturing process stemming from the interfacial side reactions between water molecules and cathode materials. The relevant chemical reaction is described in the equation[5] below (1).

$$Li_xM_yO_z + pH_2O \rightleftharpoons H_pLi_{x-p}M_yO_z + pLi^+ + (p)OH^- \quad (1)$$

As indicated in this equation, H_2O dissociates into H^+ and OH^-, and H^+ tends to spontaneously exchange with Li^+ at the cathode material surfaces, resulting in undesired Li^+ leaching and structural degradation ($H_pLi_{x-p}M_yO_z$) of the cathode materials[6] (Fig. 1a, left). In addition, the simultaneous generation of OH^- increases the pH of the slurries, inducing the surface passivation of the cathode materials and corrosion of Al current collectors[7]. The adverse effects of water molecules are particularly significant in high-capacity and high-voltage cathode materials[8].

Previous works implemented to resolve these problems have focused on modifying the surface of cathode materials[9], adding mild organic acids for in situ surface coating[10], increasing Li^+ concentration in water to reduce Li^+ leaching (Le Chatelier's principle)[5,11], and applying coatings on Al current collectors[7]. Despite these efforts, the underlying challenge of water's inherent chemical reactivity with cathode materials remains unresolved. To address this limitation and enable the use of water as a processing solvent for cathode manufacturing, it is crucial to understand and manipulate the local hydration environment around the cathode materials.

Herein, we introduce a class of aqueous processing solutions based on the kosmotropic effect, a phenomenon common in

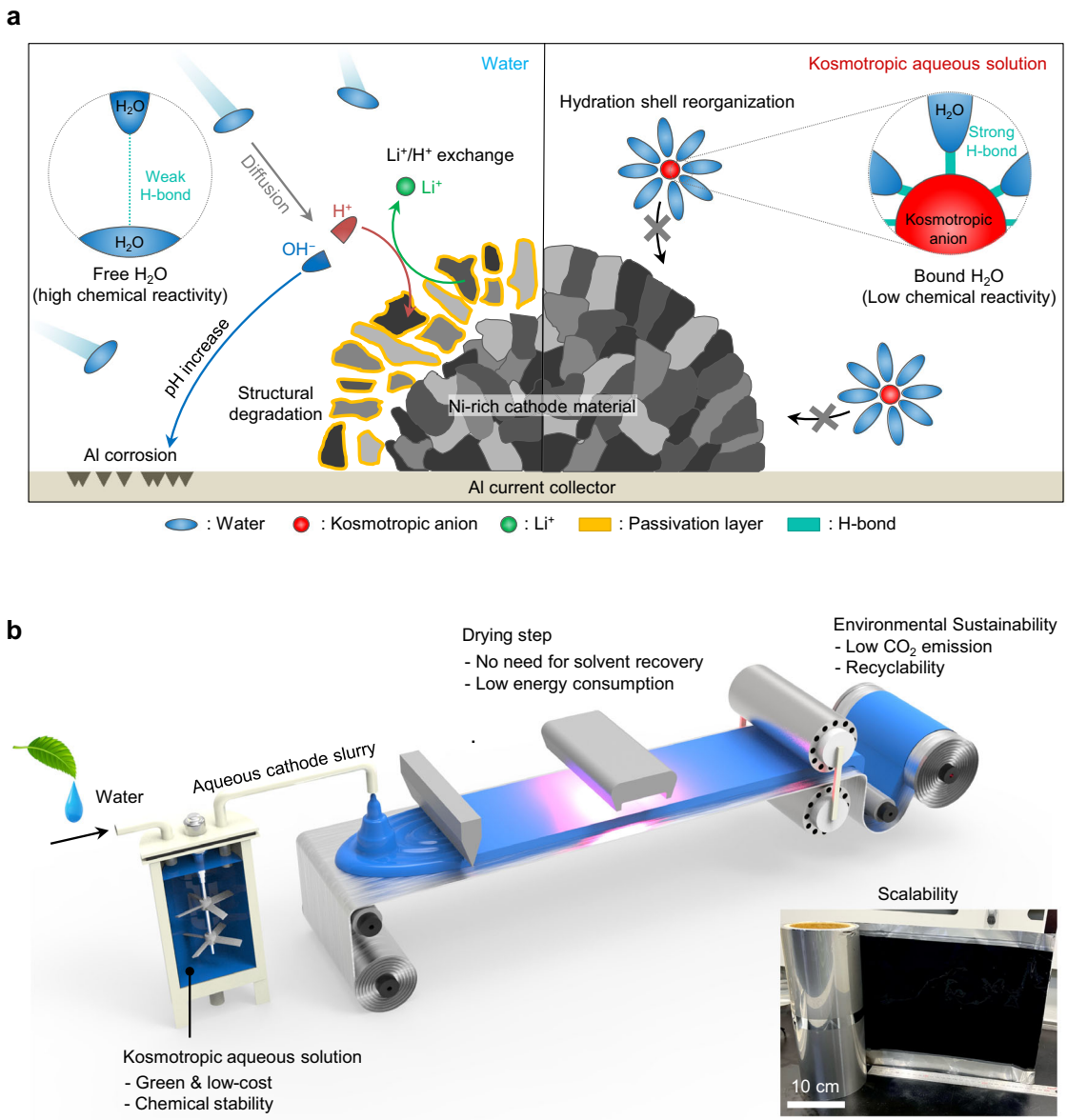

Fig. 1 | Cathode manufacturing using aqueous processing solution based on kosmotropic effect. a Interfacial side reaction between water and cathode materials during aqueous electrode processing: water (left) vs. kosmotropic aqueous solution (right). **b** Schematic of the cathode manufacturing process using kosmotropic aqueous processing solution and a photograph of the obtained cathode.

biochemistry[12,13], but rarely applied to batteries. Incorporating the kosmotropic anions resulted in the restructuring of the ion hydration shell to form a highly ordered state of anion–water clusters and the regulation of the local hydration structure adjacent to cathode materials (Fig. 1a, right). This reorganization of the ion hydration shell influences water molecules' thermodynamics and physicochemical properties, thus mitigating the undesired interfacial reactions at the cathode material surfaces during cathode fabrication.

Owing to these advantageous effects, the kosmotropic aqueous processing solution enabled the scalable slurry-cast fabrication of various Ni-rich cathodes ($LiNi_{0.6}Co_{0.2}Mn_{0.2}O_2$ (NCM622), $LiNi_{0.8}Co_{0.1}Mn_{0.1}O_2$ (NCM811), and $LiNi_{0.9}Co_{0.05}Mn_{0.05}O_2$ (NCM9½½)) with stable cycle life comparable to those of conventional NMP-processed cathodes (Fig. 1b). In addition, the kosmotropic solution-processed Ni-rich cathodes exhibited high specific and areal capacities (≥ 195 mAh g^{-1} and 3.6 mAh cm^{-2}, respectively) compared to previously reported aqueous solution-processed cathodes. In addition to the electrochemical benefits, the material cost of the kosmotropic solution is 96% lower than that of the NMP processing solvent. From a comprehensive techno-economic analysis, we propose that the use of the kosmotropic aqueous processing solution can reduce the operational (~ 23%), and capital (~ 95%) costs associated with cathode manufacturing by eliminating the conventional solvent recovery process. Furthermore, this approach substantially reduced energy consumption in electrode manufacturing by 46%, demonstrating its viability as a platform technology for environmentally friendly and cost-competitive electrode manufacturing applicable to various high-capacity electrode materials.

Results

Reorganization of ion hydration shells via Hofmeister effect

Water, comprised of two hydrogen atoms and one oxygen atom, is one of the most elementary molecules on Earth[14]. Despite its simple molecular structure, water forms intricate and dynamic configurations via extensive hydrogen bond (H-bond) networks, adopting an open tetrahedral arrangement, unlike other liquids with non-directional van der Waals interactions[15].

Ions, as categorized by the Hofmeister series, can influence the molecular structure and dynamics of water by altering the strength of its H-bond network[16]. The kosmotropic ion exhibits a high charge density and can strengthen the H-bond structure[17]. On the other side of the series, the chaotropic ion has a large and charge-delocalized molecular structure[18], exhibiting weaker intermolecular interactions with water and disordering the H-bond networks[17]. Owing to its molecular polarity, anions exert a more pronounced influence on the structure of water than cations[19]. Based on the kosmotropicity of anions, we investigated the effects of four representative Li salts: Li bis(trifluoromethanesulfonyl)imide (LiTFSI), Li trifluoromethanesulfonate (LiOTf), Li acetate (LiOAc), and Li sulfate (Li_2SO_4). Among various cation candidates, Li^+ was selected to effectively suppress the Li^+/H^+ exchange reaction in Eq. (1) described above.

To gain insight into the hydration states of these anions, we calculated their electrostatic potential (ESP) values using density functional theory (DFT) (Fig. 2a). The dipole moment in water molecules causes the preferential coordination of H atoms (H-bond donors) with the highly electronegative sites of anions (e.g., O atoms as H-bond acceptors)[20,21]. The DFT calculations revealed that the ESP values of the hydration shells gravitated towards more negative values with an increase in the kosmotropicity of anions. It is expected that the fluoroalkyl group of $TFSI^-$ or OTf^- can act as an electron-withdrawing group, reducing the electron density of the O atoms. In contrast, the methyl group of OAc^- is a weak electron-donating group, resulting in a relatively higher electron density around the O atoms. In SO_4^{2-}, the electronegativity difference between sulfur (2.58) and oxygen (3.44) causes electron density towards the oxygen atoms, resulting in a higher electron density around the O atoms. Therefore, the ability of H-bond acceptors is strengthened in the order: $TFSI^- < OTf^- < OAc^- < SO_4^{2-}$.

The structural rearrangement of anion–water clusters via H-bonds was elucidated by monitoring the molecular dynamics (MD) trajectories (Fig. 2b). The average number of H-bonds and the interaction energies with water molecules increased with the kosmotropicity of the anions (Fig. 2c). Particularly, the H-bond number and interaction energy of SO_4^{2-} with water molecules were 2.5 and 13.7 times higher than those of the chaotropic $TFSI^-$.

The strength of H-bond networks was assessed by probing the O–H stretching vibrational energies via Fourier transform infrared (FT-IR) spectroscopy (Fig. 2d). The FT-IR analysis revealed an increase in strong H-bond (~ 3200 cm^{-1}) and a corresponding decrease in weak H-bonds (~ 3600 cm^{-1}) with an increase in the kosmotropicity of anions[22]. This trend was quantitatively confirmed using the Hildebrand solubility parameter, which captures the cohesive interactions among solution components[23] (Supplementary Fig. 2 and Supplementary Note 1). These findings confirm that the kosmotropic anions restructured the ion hydration shells into an ordered state.

The dynamic anion–water interaction in different H-bond networks was investigated by measuring the longitudinal relaxation time (T_1)[24] obtained from the inversion-recovery plots of ^1H nuclear magnetic resonance (^1H NMR) spectra (Fig. 2e). Equimolal aqueous solutions of Li^+ were employed to eliminate the influence of paramagnetic ^7Li nuclei, which can alter the T_1 values[25,26]. The SO_4^{2-} exhibited the lowest T_1 value, indicating the limited mobility of the water molecules in the presence of a highly kosmotropic anion[24].

Two-dimensional ^1H-^1H nuclear Overhauser effect spectroscopy (NOESY) analysis was conducted to investigate the stereochemical relationship of protons in the aqueous solutions (Fig. 2f, g). The ^1H NMR chemical shifts indicated the electronic environments of protons influenced by different H-bond networks. In the kosmotropic solution (0.5 m Li_2SO_4 in H_2O), a downfield shift was observed compared to the chaotropic solution (1.0 m LiTFSI in H_2O), reflecting a reorganization of H-bond networks from free water to more immobilized and bound water states. Notably, the appearance of NOEs in the kosmotropic solution (blue lines in Fig. 2g) provides insight into the spatial proximity (within approximately 5 Å) of protons in the structured H-bond networks. These NOE cross-peaks in the kosmotropic solution indicated the tight intermolecular associations of protons within the anion-water clusters, demonstrating stereochemical rearrangement of the H-bond networks by the kosmotropic anion.

Local hydration structures of kosmotropic/chaotropic aqueous solutions adjacent to cathode materials

To assess the extent of detrimental Li^+/H^+ exchange reactions at the interface between cathode materials and water, we investigated the local hydration structures of the aqueous solutions utilizing MD simulations. The anion–water clusters of kosmotropic aqueous solution and chaotropic aqueous solution were theoretically investigated within the distance of 10 Å from the surface of cathode materials (NCM811) (Supplementary Figs. 3, 4, Supplementary Table 1, Supplementary Note 2, and Supplementary Datas 1–16).

Analysis of the number density distribution function ($n(r)$) of water, anion, and Li^+ along the distance (r) from the NCM811 indicated that the distribution of water and Li^+ remained nearly consistent, irrespective of the anion species (Supplementary Figs. 5 and 6). The sulfur atom of SO_4^{2-} in the kosmotropic solution was notably concentrated near the surface ($r < 5.75$ Å), whereas the central nitrogen atom of $TFSI^-$ in the chaotropic solution was located in the bulk region ($r > 5.75$ Å) (Fig. 3a, top)[27]. The preferential adsorption of SO_4^{2-} on the cathode materials can be attributed to the high charge density of kosmotropic anions[28–30]. Furthermore, the charge distribution ($e(r)$) of the anions indicates that the oxygen atoms (strong H-bond acceptors) of SO_4^{2-} are predominantly located in the surface region (Fig. 3a,

https://doi.org/10.1038/s41467-025-56831-9

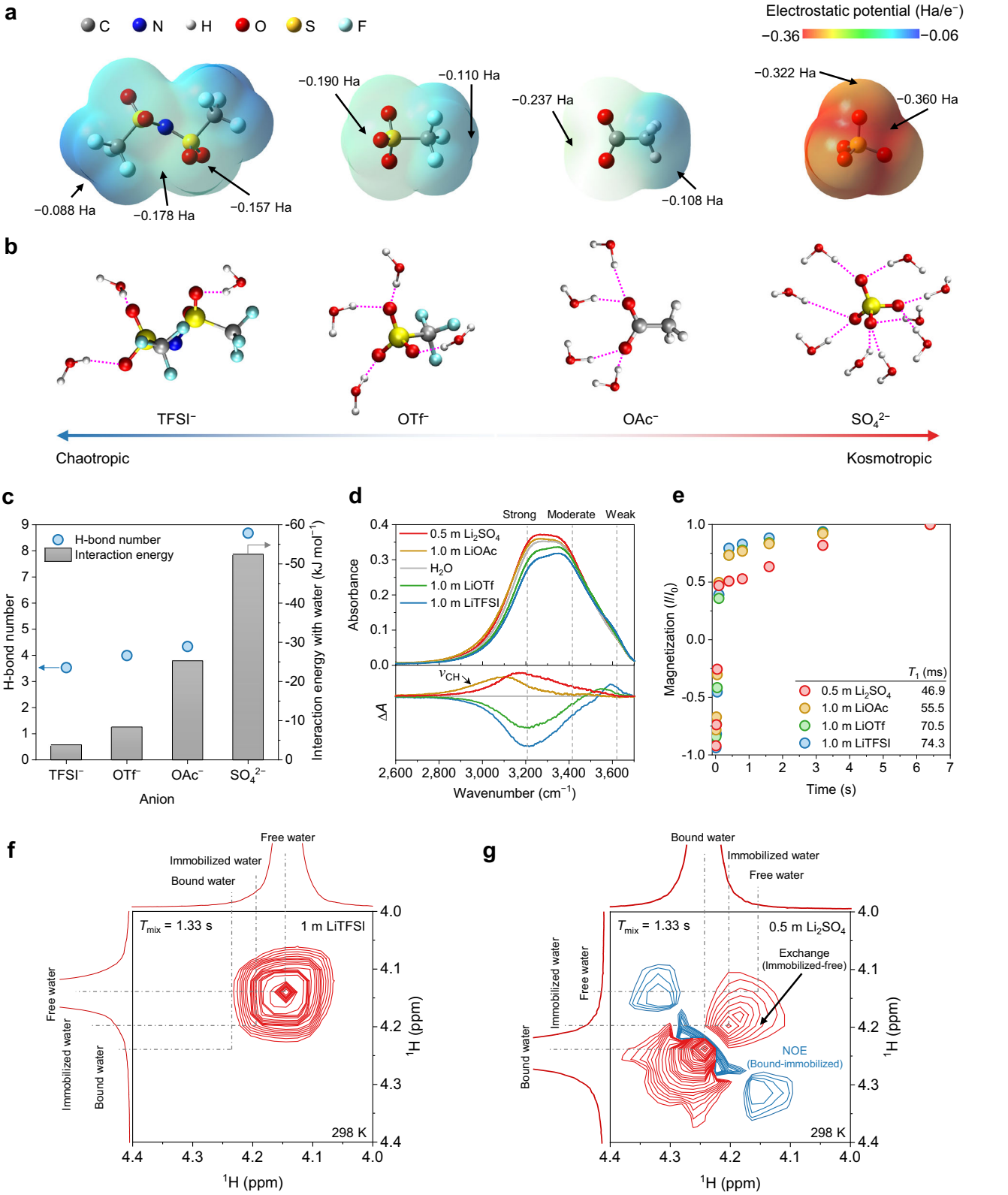

Fig. 2 | Reorganization of ion hydration shell by Hofmeister effect. **a**, **b** Electrostatic potential maps (**a**) and hydration structures (**b**) of different anions ($TFSI^-$, OTf^-, OAc^-, and SO_4^{2-}) with varying chaotropicity and kosmotropicity. Gray, blue, white, red, yellow, and cyan spheres represent carbon, nitrogen, hydrogen, oxygen, sulfur, and fluorine, respectively. **c** H-bond number of anion-water clusters and interaction energy between anion and water molecules calculated from the molecular dynamics (MD) trajectories. **d** Fourier transform infrared (FT-IR) spectra representing O–H stretching mode of aqueous solutions and absorbance difference ($\Delta A = A_x - A_{H_2O}$) under equimolal Li^+ concentration at 1.0 m. ν_{CH} indicates C–H stretching vibration of OAc^-. **e** Inversion-recovery plots of aqueous solutions obtained from ^1H NMR spectra. **f**, **g** 2D ^1H-^1H NOESY spectra of chaotropic solution (1.0 m LiTFSI in H_2O) (**f**) and kosmotropic solution (0.5 m Li_2SO_4 in H_2O) (**g**) using a mixing time (T_{mix}) of 1.33 s at 298 K. Positive phase peaks are depicted in red, and negative peaks are shown in blue with identical contour levels.

https://doi.org/10.1038/s41467-025-56831-9

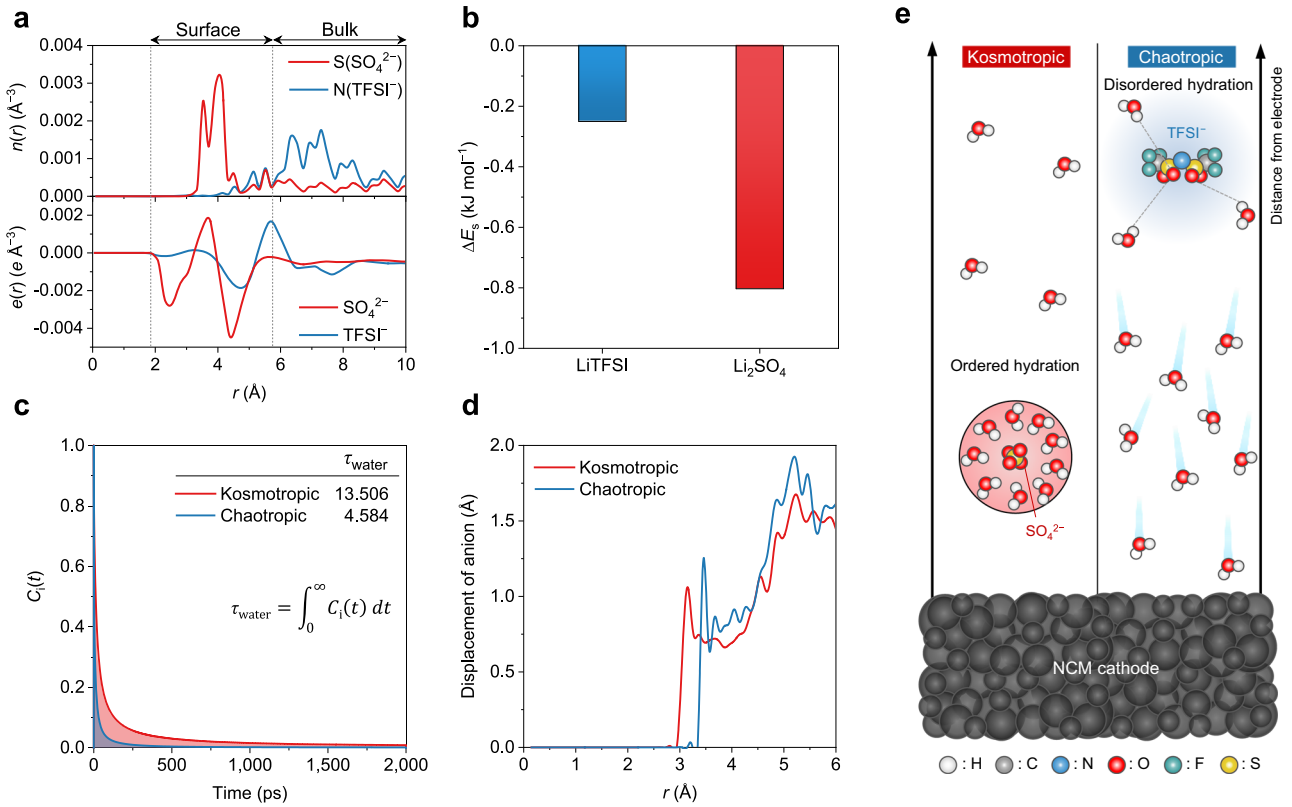

Fig. 3 | Local hydration structures of kosmotropic/chaotropic aqueous solutions adjacent to cathode materials. a Number density distribution function ($n(r)$) (top) and charge density distribution function ($e(r)$) (bottom) of anions in aqueous solutions at NCM811surface obtained from MD simulations. **b** Comparison of water stabilization energy (ΔE_s) in aqueous solutions upon addition of Li salts: LiTFSI vs. Li_2SO_4. **c** Residence time correlation function ($C_i(t)$) of water in aqueous solutions and corresponding residence time (τ_{water}) in the first coordination shell of anions. **d** Displacement of anions from the surface of NCM811 for 5 ps. **e** Schematic of the local ion hydration structure at the NCM811 surface.

bottom). Higher concentrations of SO_4^{2-} near the cathode surface can interact with reactive H^+ at the NCM811–water interface, consistent with the previously reported result for $LiCoO_2$ in salt-in-water electrolytes[30].

To further understand the impact of anions, the stability of water molecules was assessed by analyzing the shift in stabilization energy (ΔE_s)[31] (Fig. 3b and Supplementary Note 3). Compared to the chaotropic LiTFSI with a ΔE_s value of 0.25 kJ mol^{-1}, the kosmotropic Li_2SO_4 displayed a larger ΔE_s value of 0.80 kJ mol^{-1}, highlighting the role of order-making ions on the stabilization of water molecules.

The dynamics of water molecules in the surface region of NCM811 were investigated using the residence time correlation function ($C_i(t)$) from the MD trajectories (Fig. 3c). The $C_i(t)$ of water in the kosmotropic solution decayed gradually, suggesting that the kosmotropic SO_4^{2-} can establish long-lasting hydration clusters[32]. The formation of stable hydration clusters indicates a marked restriction in the free motion of water molecules. The restricted mobility was quantitatively validated by investigating water molecules' residence time (τ_{water}). The interaction of water with kosmotropic anions prolonged the residence time by a factor of 2.9 compared to the interaction with chaotropic anions.

To gain insight into the diffusion behavior of ion hydration clusters, the displacement of anions was monitored for 5 ps (Fig. 3d)[33]. Despite the low molecular weight and small radius of the geometry of SO_4^{2-} (Supplementary Fig. 7), its hydration cluster exhibited a smaller displacement than the $TFSI^-$-centered cluster. These observations confirm that the mobility of both anions and water molecules within the hydration shells was reduced in the kosmotropic solution. The ordered, long-lasting kosmotropic hydration shell is primarily located near the surface of NCM811. This modification in the local hydration structure influences the dynamics of water molecules, potentially mitigating undesired interfacial chemical reactions on the NCM811 surface (Fig. 3e).

Chemical reactivity of kosmotropic/chaotropic aqueous processing solutions with cathode materials

To understand the influence of the hydration structure of kosmotropic and chaotropic aqueous processing solutions on their chemical reactivity with cathode materials, NCM811 particles were immersed in the respective solutions and subsequently collected for analysis (Supplementary Fig. 8). First, we quantified Li^+ leaching from the NCM811 by measuring the change in the Li^+ concentration of the immersion solution using inductively coupled plasma-optical emission spectroscopy (ICP-OES) (Fig. 4a, top). The change in the Li^+ concentration of the kosmotropic solution was significantly lower than that of water or the chaotropic solution, indicating the suppression of Li^+ leaching from the NCM811.

To further assess Li^+/H^+ exchange reactions, the pH change of the immersion solutions was measured. The insertion of H^+ into NCM811 would increase the pH values of these solutions. Notably, the kosmotropic solution exhibited the smallest pH increase compared to water and the chaotropic solution (Fig. 4a, bottom). This pH increase results in the corrosion of Al current collectors, thus increasing electrochemical impedance. The surface alterations to the Al current collectors were characterized after casting electrode slurries prepared from different aqueous processing solutions (Supplementary Fig. 9). Scanning electron microscopy (SEM) images revealed numerous defects and pinholes on the current collectors exposed to the water- and chaotropic solution-based electrode slurries, which can be attributed to high OH^- concentrations. In contrast, those exposed to the

https://doi.org/10.1038/s41467-025-56831-9

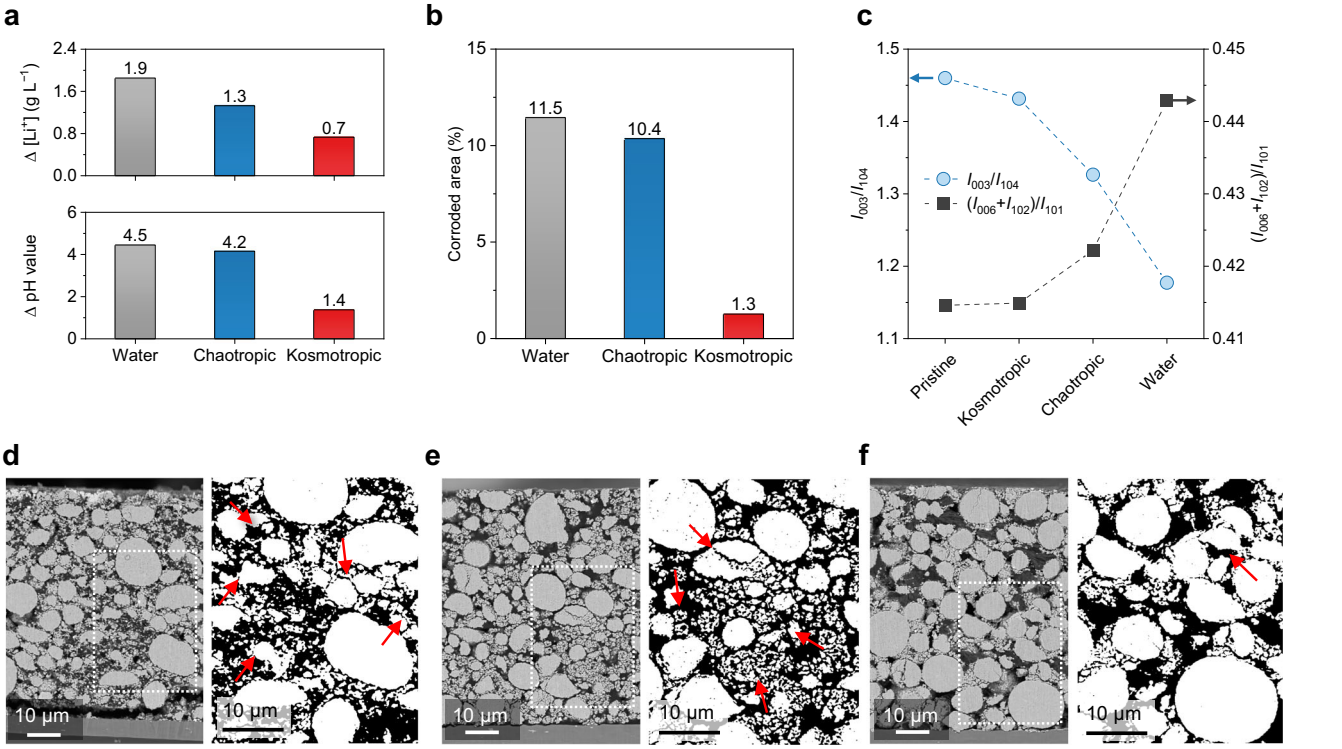

Fig. 4 | Chemical reactivity of kosmotropic/chaotropic aqueous solutions with cathode materials. a Change in Li^+ concentration (top) and pH (bottom) of aqueous solutions (from the model study presented in Supplementary Fig. 8). The Li^+ concentration of the solution was measured using ICP-OES. **b** Corroded area of the Al current collectors after exposure to various aqueous electrode slurries. The area was estimated from binary SEM images in Supplementary Fig. 9. **c** Intensity ratios of I_{003}/I_{104} and $(I_{106}+I_{102})/I_{101}$ of the NCM811 obtained via X-ray diffraction (XRD) analysis. **d**–**f** Cross-sectional scanning electron microscopy (SEM) images and corresponding binary images of aqueous solution-processed cathodes: water (**d**), chaotropic solution (**e**), kosmotropic solution (**f**). Red arrows indicate intergranular cracks of NCM811 secondary particles.

kosmotropic solution-based slurry exhibited substantially less corrosion (Fig. 4b).

The microstructural degradation of NCM811 was investigated using SEM (Supplementary Fig. 10). After immersion in the water or chaotropic solutions, the secondary NCM811 particles disintegrated into primary particles. In contrast, particles immersed in the kosmotropic solution remained relatively intact. This observation was quantitatively confirmed by analyzing particle size distribution using Zetasizer (Supplementary Fig. 11). The particle size tends to decrease in the order of NMP > kosmotropic solution > chaotropic solution > water. This finding demonstrates that the microstructural degradation of secondary NCM811 particles is ascribed to the undesired interfacial side reactions with water along the crystal grain boundaries[34].

Change in crystallinity of the rhombohedral NCM811 particles with *R*-3*m* space group was investigated using X-ray diffraction (XRD) analysis (Fig. 4c and Supplementary Fig. 12). The intensity ratio of I_{003}/I_{104}, which is inversely proportional to the degree of cation disorder, was compared[35,36]. The NCM811 particles immersed in the water and chaotropic solution exhibited low I_{003}/I_{104} intensity ratios. In contrast, the particles immersed in the kosmotropic solution displayed a high I_{003}/I_{104} intensity ratio of 1.43, similar to that of pristine NCM811 (1.46). The hexagonal ordering of the particles was investigated by comparing the $(I_{006}+I_{102})/I_{101}$ ratios[37,38]. The NCM811 particles in the kosmotropic solution exhibited reduced $(I_{006}+I_{102})/I_{101}$ values compared to those in water and the chaotropic solutions, indicating the stabilization of hexagonal ordering within the crystal lattice. These results demonstrate the effectiveness of the kosmotropic solution in preserving the structural stability of the NCM811 particles.

Electrochemical performance of cathodes manufactured with aqueous processing solutions

To test the aqueous processed cathodes, we prepared cells comprising of Li metal anodes and NMC811 cathodes with areal mass loading and electrode density densities of 18 mg_{NCM811} cm^{-2} and 3.0 g cc^{-1}, respectively (See Methods and Supplementary Table 2 for details). The aqueous cathode slurries exhibited dispersion stability similar to those formulated in NMP, suggesting that the incorporation of kosmotropic or chaotropic salts had a minimal effect on the dispersion of electrode slurries (Supplementary Fig. 13). After calendaring, the structures of the electrodes were analyzed using cross-sectional SEM and corresponding electron probe microanalyzer (EPMA) images (Supplementary Fig. 14). Intergranular cracks were observed on the NCM811 particles in the water- and chaotropic solution-processed cathodes (red arrows, Fig. 4d, e). In contrast, the particles in the kosmotropic solution-processed cathodes remained comparatively unimpaired (Fig. 4f). These observations imply that external pressures can amplify the microstructural degradation of cathode materials after the aqueous processing.

The capacity of the water-processed cathodes degraded significantly after 200 cycles because of the active Li^+/H^+ exchange[5,39] during the aqueous cathode fabrication (Supplementary Fig. 15 and Fig. 5a). The chaotropic solution-processed cathode showed improved cyclability than the water-processed cathode, however, failed to maintain the cycle retention after 300 cycles. In contrast, the kosmotropic solution-processed cathode delivered a high initial specific capacity of 205 mAh g_{NCM811}^{-1} with a stable cycle retention (over 80% after 400 cycles), which is comparable to that of the NMP-processed cathode. We analyzed the cathodes after 400 cycles using electrochemical impedance spectroscopy (EIS, Supplementary Fig. 16). The

https://doi.org/10.1038/s41467-025-56831-9

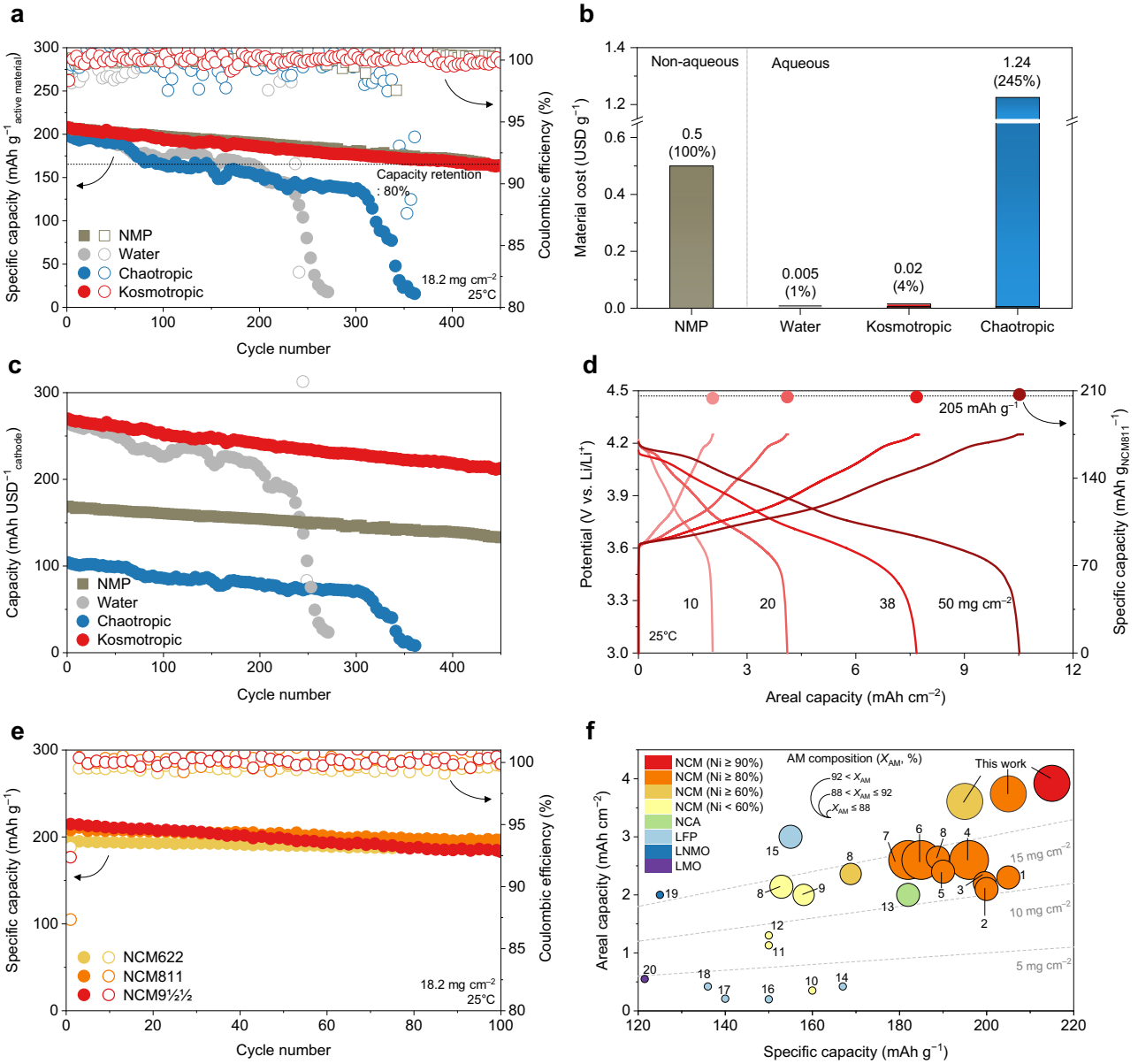

Fig. 5 | Electrochemical performance of NCM811 electrodes prepared by aqueous processing solutions. a Cycling retention (expressed as discharge-specific capacities of cathode materials) of the cathodes at a charge/discharge current rate of 0.2 C/0.5 C (1 C = 3.74 mA cm^{-2}). The cathode material mass loadings were 18.2 mg cm^{-2}. **b** Material cost of aqueous processing solutions compared to NMP (a commercial non-aqueous processing solution). **c** Cycling retention (expressed as capacities normalized by material costs) of the cathodes. **d** Galvanostatic initial charge/discharge profiles as a function of mass loading of kosmotropic solution-processed cathodes at a current rate of 0.1 C/0.1 C. These profiles were obtained after one formation cycle (0.1 C/0.1 C). **e** Cycling retention of kosmotropic solution-processed NCM622, NCM811, and NCM9½½ cathodes. The cathode material mass loadings were 18.2 mg cm^{-2}. **f** Comparison of kosmotropic solution-processed cathodes and previously reported aqueous solution-processed cathodes in terms of four parameters: specific capacity of cathode materials (x-axis), areal capacity (y-axis), types of cathode materials (heatmap), and cathode material composition (X_{AM}) of the electrode (diameter). The gray dashed lines represent the mass loading of cathode materials. The number assigned to each circle corresponds to the serial number in Supplementary Table 7 (refs. 5,10,11,39,48–61) The electrochemical tests were conducted within a voltage range of 3.00–4.25 V and at a temperature of 25 °C.

charge transfer resistance (R_{ct}) and the film resistance (R_{film}) of the kosmotropic solution-processed cathodes were comparable to those of the NMP-processed cathodes. Meanwhile, stable cycling performance (85% retention after 300 cycles) was also observed at higher Li_2SO_4 concentrations of 1.0 and 2.0 m (Supplementary Fig. 17).

The material costs of the aqueous processing solutions and NMP were analyzed in Fig. 5b (see calculation details in Supplementary Table 3). The kosmotropic Li_2SO_4 salt (0.33 USD g^{-1}) is more cost-effective than the chaotropic LiTFSI salt (5.52 USD g^{-1}) owing to its elemental abundance and ease of synthesis: the cost of the kosmotropic solution (0.02 USD g^{-1}) is merely 4% of the price of NMP. Fig. 5c demonstrates that the kosmotropic solution-processed NCM811 cathode can achieve higher capacities normalized by the material costs over the entire cycles, surpassing the NMP-processed cathode (see calculation details in Supplementary Table 4). This material cost-normalized capacity interpretation highlights a significant economic and performance advantage over current NMP-based cathode manufacturing.

To address potential concerns regarding the presence of precipitated kosmotropic/chaotropic salts in the aqueous solution-processed cathodes, we estimated the specific capacities of the cathodes based on their total mass, including the mass of the precipitated

salts (Supplementary Fig. 18 and Supplementary Table 5). Owing to the low molar mass of Li_2SO_4 (55.0 g mol_{Li}^{-1}), the kosmotropic solution-processed cathode achieved a specific capacity of 159 mAh $g_{cathode}^{-1}$, closely mirroring the NMP-processed cathode (162 mAh $g_{cathode}^{-1}$). Meanwhile, the chaotropic solution yielded a diminished specific capacity of 142 mAh $g^{-1}_{cathode}$, which can be attributed to the heavier LiTFSI salt (287.1 g mol_{Li}^{-1}).

Furthermore, the kosmotropic solution-processed cathode delivered up to 188 mAh g^{-1} under a fixed charge current density of 3.0 mA cm^{-2}, comparable to the NMP-processed cathode (Supplementary Fig. 19). In contrast, the chaotropic solution-processed cathodes exhibited inferior performance, which can be ascribed to the pore blockage as shown in the cross-sectional SEM images (Supplementary Fig. 20) and the reduced particle size of NCM811 that could increase the tortuosity of ion conduction (Supplementary Fig. 11). In contrast, the kosmotropic solution-processed cathode maintained a porous structure. Energy-dispersive spectroscopy (EDS) mapping further confirms the dense distribution of O atoms in the through-thickness direction of the cathode, originating from the precipitated LiTFSI salt. This result is consistent with the molar volume calculations, which revealed that the volume occupied by chaotropic LiTFSI is approximately 8.7-fold higher than that of kosmotropic Li_2SO_4 (Supplementary Table 5a). The ionic resistances of the electrodes (R_{ion}) were evaluated using EIS in a blocking-symmetric cell (electrode||electrode) configuration (Supplementary Fig. 21). Under the constrained amount (E/C ratio = 2 g Ah^{-1} per each electrode) of liquid electrolyte, which surpasses the total volume of the electrode and separator[40] (Supplementary Table 6). R_{ion} values appeared to be equilibrated after 6 h of aging, confirming complete wetting of the electrodes (Supplementary Fig. 21d). The kosmotropic solution-processed cathode exhibited a low R_{ion} (~ 7.5 Ω cm^2), closely resembling that of the water-processed cathode (~ 6.0 Ω cm^2). In contrast, the chaotropic solution-processed cathode presented a significantly high R_{ion} at ~ 80 Ω cm^2, suggesting that the increased tortuosity stemming from the blocked pores and the reduced particle size of NCM811 further hinders ion transport.

Electrochemical analysis was extended to high-areal-loading NCM811 cathodes (Fig. 5d and Supplementary Fig. 22). The kosmotropic solution-processed cathodes stably maintained the specific capacity of NCM811 (~ 205 mAh g_{NCM811}^{-1}) up to an areal mass loading of 50 mg cm^{-2} (~ 10 mAh cm^{-2}). In addition, NCM622, NCM811, and NCM9½½ processed with the kosmotropic solution achieved capacities of 195, 205, and 215 mAh g^{-1}, respectively, aligning closely with their practical capacities (Supplementary Fig. 23). The cycling stabilities of these kosmotropic solution-processed NCM cathodes are displayed in Fig. 5e, demonstrating the versatile application of the kosmotropic solution.

To highlight the improved cell performance, the kosmotropic solution-processed cathodes, and previously reported aqueous solution-processed cathodes are compared in Fig. 5f, Supplementary Fig. 24, and Supplementary Table 7. Previous studies have focused on enabling the aqueous processing of cathode materials that are less sensitive to water, including low-Ni NCM (Ni < 60%), $LiFePO_4$, $LiMn_2O_4$, and $Li_{0.5}Ni_{1.5}MnO_4$. In contrast, the kosmotropic solution-processed cathodes exhibited high specific and areal capacities (≥ 195 mAh g^{-1} and 3.6 mAh cm^{-2}). In addition, these cathodes contain high active material content (≥ 93%), meeting the requirements of practical Li batteries.

Economic and environmental analysis of kosmotropic aqueous cathode manufacturing process

To explore the practical implications of these scientific findings for industrial applications, we designed process flow diagrams (PFDs) for the manufacturing electrode with NMP solvent and kosmotropic aqueous processing solutions (Fig. 6a, Supplementary Fig. 25, Supplementary Table 8, and Supplementary Note 4). The NMP-processed cathodes were dried at high temperatures, followed by a recovery step of NMP vapor via condensation (emphasized within the dashed outline in Fig. 6a). The recycling step is imperative given the high cost of NMP and its environmental impacts upon atmospheric release, and accounts for 45% of the total energy consumption in electrode processing (including slurry mixing, coating, drying, solvent recovery) (Supplementary Tables 9, 10, and Supplementary Note 5).

In contrast, the kosmotropic solution-based process eliminates the need for a solvent recovery step. Furthermore, the drying process of the aqueous electrode consumes less energy because of its lower vapor pressure compared to NMP. Overall, the kosmotropic aqueous cathode processing results in a 97.4% decrease in energy consumption and a 97.1% reduction in CO_2 emissions compared to the NMP-based process (Fig. 6b and Supplementary Fig. 26). Considering that the electrode processing accounts for 47% of energy consumption in battery manufacturing[41], it implies that the kosmotropic aqueous electrode processing can reduce 46% of the energy consumption, demonstrating its sustainable manufacturing. Moreover, the intrinsic simplicity of kosmotropic aqueous cathode processing translates to a 95% reduction in the initial capital expenditure (Fig. 6c) and a 23% decrease in the operating costs (Fig. 6d).

The economic, environmental, and electrochemical advantages of the kosmotropic solution (0.5 m Li_2SO_4 in H_2O) over the NMP solvent are summarized in Fig. 6e. The kosmotropic solution exhibits reduced health risks, as evidenced by its favorable material hazard index of the solution (Supplementary Table 11). Moreover, the commitment to environmental compatibility is evident from the commendable green score in Supplementary Table 12. These benefits collectively contribute to a significant reduction in CO_2 emissions associated with electrode manufacturing. Utilizing the fluorine-free binder is expected to further enhance the sustainable value chain of the batteries (Supplementary Table 12b).

Discussion

The widespread use of the hazardous chemical NMP in LIB cathode manufacturing has raised significant environmental concerns. To address this imperative issue, we designed a kosmotropic aqueous processing solution to mitigate the adverse interfacial chemical reactions between water and cathode materials by forming highly ordered ion hydration shells. The kosmotropic solution-processed cathodes exhibited a stable cycle life comparable to that of the NMP-processed cathode under practical conditions and achieved their theoretical specific capacity at high areal loadings. By conducting the techno-economic analysis, we demonstrated the advantages of the kosmotropic aqueous processing solution over NMP in electrode manufacturing, achieving significant reductions in energy consumption, CO_2 emissions, and cost savings for sustainable cathode production. We anticipate that this kosmotropic solution-processed cathode approach could be extended to other electrode-active materials and battery chemistries. In addition, incorporating this kosmotropic principle into other electrode components, such as binders and conductive additives may be an effective way to mitigate water activity. This strategy provides insight into environmentally sustainable aqueous processing methodologies and encourages a path toward green and carbon-neutral battery manufacturing.

Methods

Material preparation

Lithium sulfate (Li_2SO_4, 99.5%), lithium acetate (LiOAc, 99.95%), lithium trifluoromethanesulfonate (LiOTf, 96.0%), N-methyl-2-pyrrolidone (NMP, 99.5%), carboxymethyl cellulose (CMC, M_w = 250,000, degree of substitution = 0.9), and polyacrylic acid (PAA, M_w = 45,000, purity) were purchased by Sigma-Aldrich. Lithium bis(trifluoromethanesulfonyl)imide (LiTFSI, 99.0%) and polyvinylidene fluoride (PVDF) were bought from Samchun and

https://doi.org/10.1038/s41467-025-56831-9

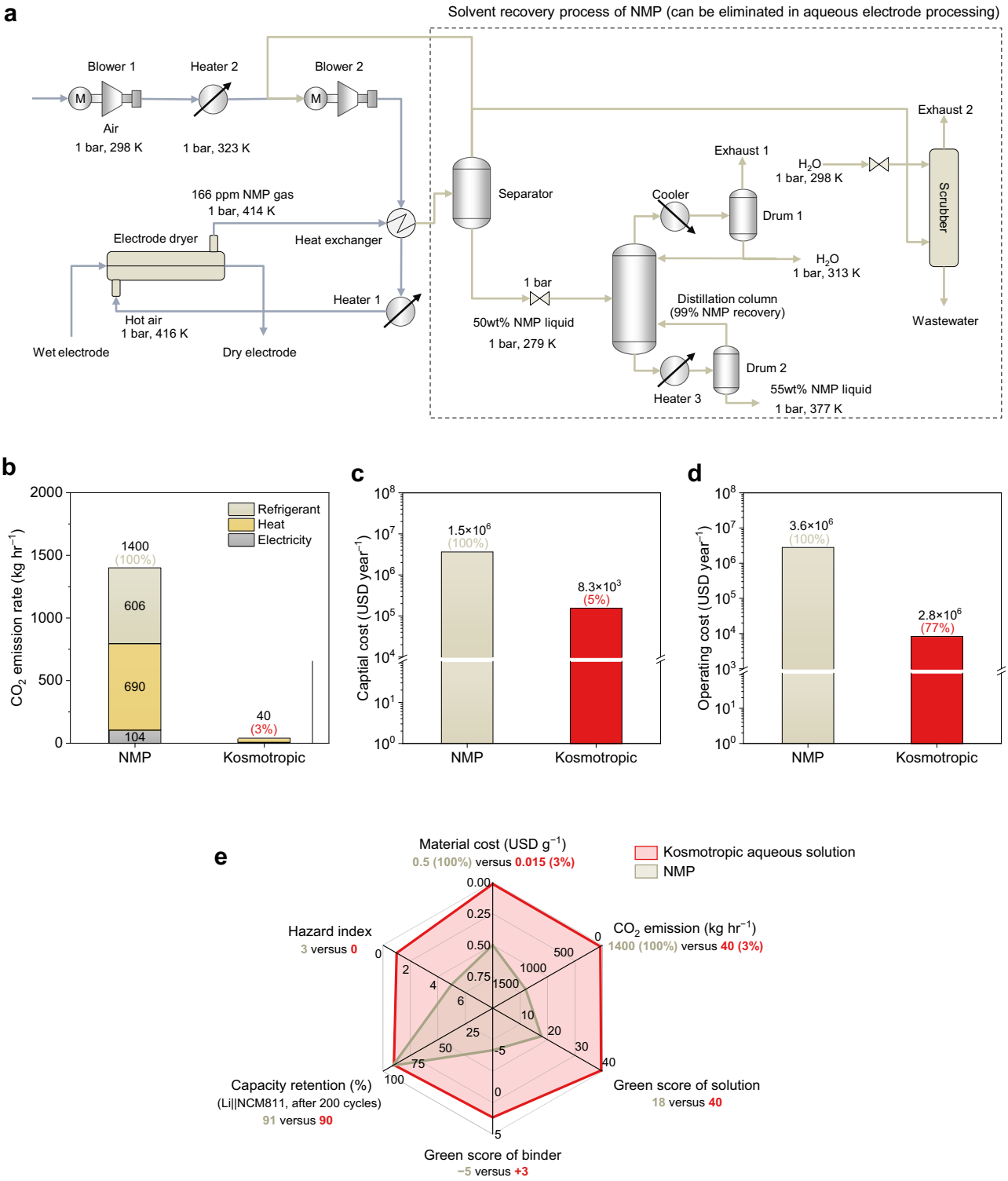

Fig. 6 | Economic and environmental analysis of the kosmotropic aqueous cathode manufacturing. a Process flow diagram of the cathode manufacturing based on the NMP solvent. **b**–**d** CO_2 emission (**b**), initial capital expenditure (**c**), and operating cost (**d**) of the cathode manufacturing process (NMP vs. kosmotropic solution). **e** Comparison of the major characteristics of the kosmotropic aqueous solution (red line) and NMP (gray line). The criteria of the hazard and green score are described in Supplementary Tables 11 and 12.

Solvay, respectively. Carbon black (Super P) powders used as a conductive additive were supplied by TIMCAL. 1 M lithium hexafluorophosphate ($LiPF_6$) in ethylene carbonate (EC)/diethyl carbonate (DEC) (= 1/1 (v/v)), fluoroethylene carbonate (FEC, 99.9%), and vinyl carbonate (VC, 99.9%) were purchased by Enchem. A water purification system (Direct Q–5UV, Merck Millipore) was utilized to prepare deionized water for aqueous processing solutions. Polyolefin (PE) separators with a porosity of 48% were provided by LG Energy solution. Li-metal were purchased from Honzo. Al current collectors were purchased from MTI. The material cost information used in Supplementary Tables 3–5 was obtained from the suppliers described above.

Structural and physicochemical characterization

The O–H stretching vibration of solutions was measured using a Fourier transform infrared (FT-IR) spectrometer (670, Varian). ^{1}H chemical shifts and longitudinal relaxation times were recorded using a 600 MHz FT NMR spectroscopy (AVANCE NEO. Bruker). ^{1}H chemical shifts were referenced to a dimethyl sulfoxide (DMSO)-d_6 as an external standard. The coaxial sample tube was used, with an inner tube containing DMSO-d_6 and an outer tube for the sample. The longitudinal relaxation time (T_1) was calculated with Eq. (2):

$$I = I_0(1 - \exp^{-t/T_1}) \quad (2)$$

where I is the peak intensity at time t, I_0 is the saturation intensity, and T_1 is the longitudinal relaxation time. The total recovery time is 6.4 s, allowing the magnetization to recover sufficiently and return to its equilibrium state, thereby minimizing saturation effects[42,43]. The ^{1}H-^{1}H NOESY spectrum was acquired by co-adding four transients for each of the 256 t1 free induction decays (FIDs) using noesygpphpp pulse sequence. A mixing time of 1.33 s and a recycle delay of 5 s were adopted. The total experimental time was approximately 3.7 h. All NMR experiments were performed at room temperature. The surface and cross-sectional morphologies of the electrodes were investigated using field emission secondary electron microscopy (FE-SEM, S-4800, Hitachi), energy-dispersive X-ray spectroscopy (EDS, JSM 6400, JEOL), and field emission electron probe microanalyzer (FE-EPMA, JXA-8530F, JEOL). To investigate the chemical reactivity of the aqueous solutions with the cathode active materials, NCM811 particles were dispersed in different processing solutions and then subjected to centrifugation to collect the treated NCM811 particles and processing solutions, respectively. Details of the analysis process are provided in Supplementary Fig. 8. The change in pH value and Li^+ concentration of the obtained processing solutions were measured using a pH meter (SevenExcellence S400, METTLER TOLEDO) and an inductively coupled plasma optical emission spectrometer (ICP-OES, 5110, Agilent), respectively. The collected particles were dried at 60 °C for 12 h, and their X-ray diffraction (XRD) patterns were recorded using an X-ray diffractometer (SmartLab, Rigaku) at 45 kV and 200 mA using Cu Kα radiation. For the particle size distribution analysis, the dried NCM811 particles were redispersed in ethanol and analyzed using a Zetasizer (ELSZneoZS, Otsuka). To observe the surface of Al current collectors after the electrode coating, the electrode active layers were gently removed from the electrode using a cotton swab soaked in dimethyl carbonate (DMC) solvent. The area of Al corrosion was quantified from binary images generated by applying 34% of the threshold program (Image J) to the SEM image of the Al current collectors. Cross-sectioned samples were thinned using a focused ion beam (FIB, Helios Nano Lab, FEI) to analyze the microstructure of NCM811 particles.

Fabrication of electrodes, cell, and electrochemical characterizations

The electrode slurries were prepared with a composition of $LiNi_{0.8}Co_{0.1}Mn_{0.1}O_2$(NCM811)/carbon black/binder = 95.5/2.0/2.5 (w/w/w). Details of the electrode composition, including residual salts, are provided in Supplementary Table 2. For aqueous solution-processed electrodes, CMC and PAA were used as binders at a composition ratio of 1/1 (w/w). The salt additives were dissolved in water for 2 h and then the CMC and PAA binders were dissolved before the formulation of electrode slurries. The binder contents in the processing solutions are 3 wt.% and 10 wt.% for CMC and PAA, respectively. No additional water is added during the electrode fabrication, leaving 47 wt.% of water in the kosmotropic electrode slurry. The electrode slurries were cast onto Al current collectors and dried at 60 °C for 6 h, followed by roll-pressing at 120 °C. The electrode fabrication process was identical regardless of the mass loading and type of cathode materials. For the NMP-processed electrodes, PVDF was used as the binder, and dissolved in NMP. The concentration of the binder solution was set at 10 wt.%. The electrode slurries were cast onto Al current collectors and dried at 120 °C for 6 h and then roll-pressed at 120 °C. The density of the fabricated electrodes was set to 3.0 g cc^{-1}, and the electrodes were vacuum dried at 120 °C for 12 h before the cell assembly.

For the electrochemical tests, CR2032 coin-type cells (Li-metal anode (thickness = 100 μm and diameter = 16 mm)|polyethylene (PE) (thickness = 16 μm and diameter = 18 mm)|Ni-rich cathode (diameter = 12 mm)) were assembled in an Ar-filled glove box. Thereafter, 1 M $LiPF_6$ in EC/DEC)(= 1/1 (v/v)) with 10 wt.% of FEC and 2 wt.% VC was used as a liquid electrolyte. The electrolyte was injected into the cell with an electrolyte mass/electrode capacity (E/C) ratio of 5 g Ah^{-1} to explore the cell performance for practical energy-dense Li-metal cells[40], if not specified. After the cell assembly, a rest period of 12 h was allowed to ensure complete wetting of the electrodes. The cells were then subjected to one formation cycle at a current rate of 0.1 C (1 C = x mA $g^{-1}_{\text{active material}}$ (x = 195, 205, and 215 for NCM622, NCM811, and NCM 9½½ active material, respectively). The cells were cycled at a charge/discharge current rate of 0.2 C/0.5 C and a voltage range of 3.00–4.25 V in 25 °C environmental chamber, if not specified. The resistances of the electrodes were measured using electrochemical impedance spectroscopy (EIS) analysis in a frequency range that varies from 10^6 to 10^{-2} Hz and an applied voltage amplitude of 10 mV using potentiostat (VSP-300, Bio-Logic). 10 points per decade of frequency were acquired. The EIS analysis of the full cells was conducted after discharge and rest at an open-circuit voltage (OCV) for 1 h. To analyze the ion resistance inside the electrodes (R_{ion}), a symmetric cell configuration (electrode||electrode) at a fully lithiated state was used. The charge/discharge performance of the cells was investigated using a cycle tester (PESC 05, PNE Solution).

Density functional theory calculations

All density functional theory (DFT) calculations of anions (i.e., $TFSI^-$, OAc^-, OTf^-, and SO_4^{2-}) were performed using the Gaussian 16 program. Becke, 3-parameter, Lee-Yang-Parr (B3LYP) hybrid functional[44,45] and Valence triple-zeta polarization basis set (def2-TZVP) basis sets[46] were used for all calculations with the Conductor-like Polarizable Continuum Model[47] (CPCM) for the water solvation effect. The self-consistent field (SCF) was converged to $1.0e^{-6}$ E_h. The geometry optimization convergence threshold was set to $4.5e^{-4}$ E_h/bohr for maximum force, $3.0e^{-4}$ E_h/bohr for root mean square (RMS) force, $1.8e^{-3}$ bohr for maximum displacement, and $1.2e^{-3}$ bohr for RMS displacement. Electrostatic potential maps were generated using Gaussview with a surface isovalue of 0.0004 and an energy value range of −0.06 E_h to −0.364 E_h.

Molecular dynamics simulations

All-atom simulations were performed to confirm the kosmotropic/chaotropic anion effect on the aqueous solutions. Each bulk aqueous solution comprised 4476 water molecules and 80 LiX molecules (X: $TFSI^-$, OAc^-, and OTF^-) to set 1 N Li^+ concentration. In the Li_2SO_4 bulk solution system, 4476 water molecules and 40 Li_2SO_4 molecules were used. The solvent system was composed of 4476 water molecules as a control group. LiTFSI, Li_2SO_4 bulk solutions, and solvent system were placed on the z-axis surface of the NCM811 cathode for the cathode-electrolyte interphase (CEI) system. The x and y dimensions of the CEI system were fixed at those of the NCM811 cathode shown in Supplementary Fig. 4 (47.960 and 45.284 Å, respectively). To prevent interactions between the solution and the NCM811 cathode above the periodic boundary conditions, a vacuum layer of 50 Å was added to the system along the z-axis. An 80 ns NVT production run was performed at 298 K after a 10 ns NPT run for the bulk system. For the CEI system, a 10 ns NVT run was performed at 353 K, after which 50 ns NVT production run was conducted.

To calculate the stabilization energy of water in the surface region, solutions were positioned only on the surface region of the NCM811 cathode. For the surface electrolyte system, the kosmotropic

solution used for the stabilization energy calculation comprised 363 H_2O molecules and 1 Li_2SO_4 molecule, whereas the chaotropic solution was comprised of 360 H_2O molecules and 2 LiTFSI molecules. The lower number of water molecules in the chaotropic solution is because the $TFSI^-$ ion is larger, occupying more area. The total system comprised the solutions on top of the NCM811 cathode. The NVT production run was performed at 298 K after a 10 ns NPT run for surface bulk systems. After running a 10 ns NVT run at 353 K, a 20 ns NVT production run was performed for the total system. The detailed information is described in the supplementary information.

Data availability

The data generated in this study are provided in the Supplementary Information and Source Data. All other data are available from the corresponding author upon request. Source data are provided in this paper.

References

1. Degen, F., Winter, M., Bendig, D. & Tübke, J. Energy consumption of current and future production of lithium-ion and post lithium-ion battery cells. *Nat. Energy* **8**, 1284–1295 (2023).
2. Sherwood, J., Farmer, T. J. & Clark, J. H. Catalyst: Possible consequences of the N-methyl pyrrolidone REACH restriction. *Chem* **4**, 2010–2012 (2018).
3. Lu, Y. et al. Dry electrode technology, the rising star in solid-state battery industrialization. *Matter* **5**, 876–898 (2022).
4. Bresser, D., Buchholz, D., Moretti, A., Varzi, A. & Passerini, S. Alternative binders for sustainable electrochemical energy storage–the transition to aqueous electrode processing and bio-derived polymers. *Energy Environ. Sci.* **11**, 3096–3127 (2018).
5. Dienwiebel, I. et al. Enabling aqueous processing for $LiNi_{0.5}Mn_{1.5}O_4$-based positive electrodes in Lithium-Ion batteries by applying Lithium-based processing additives. *Adv. Energy Sustain. Res.* **2**, 2100075 (2021).
6. Zhang, X., Jiang, W., Zhu, X., Mauger, A. & Julien, C. Aging of $LiNi_{1/3}Mn_{1/3}Co_{1/3}O_2$ cathode material upon exposure to H_2O. *J. Power Sources* **196**, 5102–5108 (2011).
7. Doberdò, I. et al. Enabling aqueous binders for lithium battery cathodes–Carbon coating of aluminum current collector. *J. Power Sources* **248**, 1000–1006 (2014).
8. Hawley, W. B. et al. Lithium and transition metal dissolution due to aqueous processing in lithium-ion battery cathode active materials. *J. Power Sources* **466**, 228315 (2020).
9. Hofmann, M., Nagler, F., Kapuschinski, M., Guntow, U. & Giffin, G. A. Surface modification of $LiNi_{0.8}Co_{0.15}Al_{0.05}O_2$ particles via Li_3PO_4 coating to enable aqueous electrode processing. *ChemSusChem* **13**, 5962–5971 (2020).
10. Loeffler, N. et al. situ coating of $Li[Ni_{0.33}Mn_{0.33}Co_{0.33}]O_2$ particles to enable aqueous electrode processing. *ChemSusChem* **9**, 1112–1117 (2016).
11. Heidbüchel, M. et al. Enabling aqueous processing of Ni-Rich layered oxide cathode materials by addition of Lithium Sulfate. *ChemSusChem* **16**, e202202161 (2023).
12. Cacace, M., Landau, E. & Ramsden, J. The Hofmeister series: salt and solvent effects on interfacial phenomena. *Q. Rev. Biophys.* **30**, 241–277 (1997).
13. Jungwirth, P. & Cremer, P. S. Beyond hofmeister. *Nat. Chem.* **6**, 261–263 (2014).
14. Marcus, Y. Effect of ions on the structure of water: structure making and breaking. *Chem. Rev.* **109**, 1346–1370 (2009).
15. Rezaei-Ghaleh, N. Water dynamics in highly concentrated salt solutions: A multi-nuclear NMR approach. *ChemistryOpen* **11**, e202200080 (2022).
16. Hofmeister, F. Zur lehre von der wirkung der salze: zweite mittheilung. *Arch. Exp. Pathol. Pharmakol.* **24**, 247–260 (1888).
17. Collins, K. D. & Washabaugh, M. W. The Hofmeister effect and the behaviour of water at interfaces. *Q. Rev. Biophys.* **18**, 323–422 (1985).
18. Assaf, K. I. & Nau, W. M. The chaotropic effect as an assembly motif in chemistry. *Angew. Chem. Int. Ed.* **57**, 13968–13981 (2018).
19. Collins, K. D. Charge density-dependent strength of hydration and biological structure. *Biophys. J.* **72**, 65–76 (1997).
20. Murray, J. S. & Politzer, P. Correlations between the solvent hydrogen-bond-donating parameter. alpha. and the calculated molecular surface electrostatic potential. *J. Org. Chemistry* **56**, 6715–6717 (1991).
21. Pike, S. J., Hutchinson, J. J. & Hunter, C. A. H-bond acceptor parameters for anions. *J. Am. Chem. Soc.* **139**, 6700–6706 (2017).
22. Cheng, F. et al. FTIR analysis of water structure and its influence on the flotation of arcanite (K_2SO_4) and epsomite ($MgSO_4 \cdot 7H_2O$). *Int. J. Miner. Process.* **122**, 36–42 (2013).
23. Kim, W.-Y. et al. Demixing the miscible liquids: toward biphasic battery electrolytes based on the kosmotropic effect. *Energy Environ. Sci.* **15**, 5217–5228 (2022).
24. Lever, M., Blunt, J. & Maclagan, R. Some ways of looking at compensatory kosmotropes and different water environments. *Comp. Biochem. Physiol. Part A: Mol. Integr. Physiol.* **130**, 471–486 (2001).
25. Febrian, R., Roddy, J. P., Chang, C. H., Devall, C. T. & Bracher, P. J. Removal of paramagnetic ions prior to analysis of organic reactions in aqueous solutions by NMR spectroscopy. *ACS Omega* **6**, 14727–14733 (2021).
26. Kocman, V., Di Mauro, G. M., Veglia, G. & Ramamoorthy, A. Use of paramagnetic systems to speed-up NMR data acquisition and for structural and dynamic studies. *Solid State Nucl. Magn. Reson.* **102**, 36–46 (2019).
27. Xing, L., Vatamanu, J., Borodin, O., Smith, G. D. & Bedrov, D. Electrode/electrolyte interface in sulfolane-based electrolytes for Li ion batteries: a molecular dynamics simulation study. *J. Phys. Chem. C* **116**, 23871–23881 (2012).
28. Hu, Z., Vatamanu, J., Borodin, O. & Bedrov, D. A comparative study of alkylimidazolium room temperature ionic liquids with FSI and TFSI anions near charged electrodes. *Electrochim. Acta* **145**, 40–52 (2014).
29. Dourado, A. H. Electric double layer: The good, the bad, and the beauty. *Electrochem* **3**, 789–808 (2022).
30. Oh, H. et al. Anion-induced interfacial liquid layers on LiCoO2 in salt-in-water Lithium-Ion batteries. *JACS Au* **3**, 1392–1402 (2023).
31. Boys, S. F. & Bernardi, F. The calculation of small molecular interactions by the differences of separate total energies. *Some procedures reduced errors. Mol. Phys.* **19**, 553–566 (1970).
32. Zhang, Y. & Maginn, E. J. Direct correlation between ionic liquid transport properties and ion pair lifetimes: A molecular dynamics study. *J. Phys. Chem. Lett.* **6**, 700–705 (2015).
33. Kim, J. et al. Observation of H_2 evolution and electrolyte diffusion on MoS_2 monolayer by in situ liquid-phase transmission electron microscopy. *Adv. Mater.* **34**, 2206066 (2022).
34. Azhari, L. et al. Effects of extended aqueous processing on structure, chemistry, and performance of polycrystalline LiNixMnyCozO_2 Cathode Powders. *ACS Appl. Mater. Interfaces* **12**, 57963–57974 (2020).
35. Li, T. et al. Degradation mechanisms and mitigation strategies of nickel-rich NMC-based lithium-ion batteries. *Electrochem. Energy Rev.* **3**, 43–80 (2020).
36. Hua, W. et al. Na-doped Ni-rich $LiNi_{0.5}Co_{0.2}Mn_{0.3}O_2$ cathode material with both high rate capability and high tap density for lithium ion batteries. *Dalton Tran* **43**, 14824–14832 (2014).
37. Dahn, J., von Sacken, U. & Michal, C. Structure and electrochemistry of $Li_{1\pm y}NiO_2$ and a new Li2NiO2 phase with the Ni (OH) 2 *Structure. Solid State Ion* **44**, 87–97 (1990).
38. Reimers, J., Rossen, E., Jones, C. & Dahn, J. Structure and electrochemistry of $Li_xFe_yNi_1$-yO_2. *Solid State Ion* **61**, 335–344 (1993).
39. Ibing, L. et al. The role of the pH value in water-based pastes on the processing and performance of Ni-rich LiNi0. 5Mn0. 3Co0. 2O2 based positive electrodes. *J. Power Sources* **475**, 228608 (2020).

40. Xue, W. et al. Ultra-high-voltage Ni-rich layered cathodes in practical Li metal batteries enabled by a sulfonamide-based electrolyte. *Nat. Energy* **6**, 495–505 (2021).
41. Liu, Y., Zhang, R., Wang, J. & Wang, Y. Current and future lithium-ion battery manufacturing. *iScience* **24**, 102332 (2021).
42. Claridge, T. D. *High-resolution NMR techniques in organic chemistry*. Vol. 27 (Elsevier, 2016).
43. Keeler, J. *Understanding NMR spectroscopy*. (John Wiley & Sons, 2010).
44. Stephens, P. J., Devlin, F. J., Chabalowski, C. F. & Frisch, M. J. Ab initio calculation of vibrational absorption and circular dichroism spectra using density functional force fields. *J. Phys. Chem.* **98**, 11623–11627 (1994).
45. Raghavachari, K. Perspective on density functional thermochemistry. III. *role exact exchange*. *J. Chem. Phys.* **98**, 5648–5652 (1993).
46. Weigend, F. & Ahlrichs, R. Balanced basis sets of split valence, triple zeta valence and quadruple zeta valence quality for H to Rn: Design and assessment of accuracy. *Phys. Chem. Chem. Phys.* **7**, 3297–3305 (2005).
47. Barone, V. & Cossi, M. Quantum calculation of molecular energies and energy gradients in solution by a conductor solvent model. *J. Phys. Chem. A* **102**, 1995–2001 (1998).
48. Kuo, J.-H. & Li, C.-C. Water-based process to the preparation of nickel-rich Li $(Ni_{0.8}Co_{0.1}Mn_{0.1})O_2$ cathode. *J. Electrochem. Soc* **167**, 100504 (2020).
49. Radloff, S., Scurtu, R.-G., Hölzle, M. & Wohlfahrt-Mehrens, M. Applying established water-based binders to aqueous processing of $LiNi_{0.83}Co_{0.12}Mn_{0.05}O_2$ positive electrodes. *J. Electrochem. Soc* **168**, 100506 (2021).
50. Radloff, S., Scurtu, R.-G., Hölzle, M. & Wohlfahrt-Mehrens, M. Water-based $LiNi_{0.83}Co_{0.12}Mn_{0.05}O_2$ electrodes with excellent cycling stability fabricated using unconventional binders. *J. Electrochem. Soc.* **169**, 040514 (2022).
51. Wood, M. et al. Chemical stability and long-term cell performance of low-cobalt, Ni-Rich cathodes prepared by aqueous processing for high-energy Li-Ion batteries. *Energy Stor. Mater.* **24**, 188–197 (2020).
52. Hofmann, M., Kapuschinski, M., Guntow, U. & Giffin, G. A. Implications of aqueous processing for high energy density cathode materials: part I. Ni-rich layered oxides. *J. Electrochem. Soc.* **167**, 140512 (2020).
53. Chen, Z. et al. Toward greener lithium-ion batteries: Aqueous binder-based $LiNi_{0.4}Co_{0.2}Mn_{0.4}O_2$ cathode material with superior electrochemical performance. *J. Power Sources* **372**, 180–187 (2017).
54. Loeffler, N. et al. Performance of $LiNi_{1/3}Mn_{1/3}Co_{1/3}O_2$/graphite batteries based on aqueous binder. *J. Power Sources* **248**, 915–922 (2014).
55. Hofmann, M., Nagler, F., Guntow, U., Sextl, G. & Giffin, G. A. Long-term cycling performance of aqueous processed Ni-rich $LiNi_{0.8}Co_{0.15}Al_{0.05}O_2$ cathodes. *J. Electrochem. Soc.* **168**, 060511 (2021).
56. Li, J., Armstrong, B. L., Kiggans, J., Daniel, C. & Wood, D. L. Lithium ion cell performance enhancement using aqueous $LiFePO_4$ cathode dispersions and polyethyleneimine dispersant. *J. Electrochem. Soc.* **160**, A201 (2012).
57. Ye, R., Hamzelui, N., Ihrig, M., Finsterbusch, M. & Figgemeier, E. Water-Based Fabrication of a $Li|Li_7La_3Zr_2O_{12}|LiFePO_4$ Solid-State Battery— Toward Green Battery Production. *ACS Sustain. Chem. Eng.* **10**, 7613–7624 (2022).
58. Lux, S., Schappacher, F., Balducci, A., Passerini, S. & Winter, M. Low cost, environmentally benign binders for lithium-ion batteries. *J. Electrochem. Soc.* **157**, A320 (2010).
59. Li, C.-C., Lee, J.-T., Lo, C.-Y. & Wu, M.-S. Effects of PAA-NH_4 addition on the dispersion property of aqueous $LiCoO_2$ slurries and the cell performance of as-prepared $LiCoO_2$ cathodes. *Electrochem. Solid-State Lett* **8**, A509 (2005).
60. Porcher, W., Lestriez, B., Jouanneau, S. & Guyomard, D. Optimizing the surfactant for the aqueous processing of $LiFePO_4$ composite electrodes. *J. Power Sources* **195**, 2835–2843 (2010).
61. Ryou, M.-H., Hong, S., Winter, M., Lee, H. & Choi, J. W. Improved cycle lives of $LiMn_2O_4$ cathodes in lithium ion batteries by an alginate biopolymer from seaweed. *J. Mater. Chem. A* **1**, 15224–15229 (2013).

Acknowledgements

This work was supported by the Basic Science Research Program through the National Research Foundation of Korea (NRF) funded by the Ministry of Science and ICT (RS-2024-00344021 and RS-2024-00455177), HRD Program for Industrial Innovation (RS-2024-00420590), and Ministry of Education (RS-2023-00273623). This work was also supported by the Samsung Research Funding Center of Samsung Electronics project number SRFC-MA2202-05.

Author contributions

J.-H.K., W.-Y.K., and S.-Y.L. designed this work. J.-H.K. and W.-Y.K. performed the experimental characterization and electrochemical tests. S.B.K. and N.J.P. performed the theoretical calculations. J.D.K. performed the cost analysis of the electrode manufacturing process. S.P.H. conducted the FT NMR analysis. K.R. and S.-J.L. assisted with the data analysis. J.H.K., W.B.L., and S.-Y.L. supervised the overall project. All authors contributed to finalizing the manuscript.

Competing interests

The authors declare no competing interests.

Additional information

Supplementary information The online version contains supplementary material available at https://doi.org/10.1038/s41467-025-56831-9.

Correspondence and requests for materials should be addressed to Junghwan Kim, Won Bo Lee or Sang-Young Lee.

Peer review information *Nature Communications* thanks the anonymous reviewers for their contribution to the peer review of this work. A peer review file is available.